Journal of Inorganic and Organometallic Polymers and Materials
https://doi.org/10.1007/s10904-022-02456-0

Energy Storage Performance of Nitrogen Doped Reduced Graphene Oxide/Co-Doped Polyaniline Nanocomposites

Hasan Altınışık[1] · Bengü Getiren[2] · Zafer Çıplak[3] · Furkan Soysal[4] · Nuray Yıldız[1]

Received: 29 April 2022 / Accepted: 21 July 2022

Abstract

The design and exploration of carbon-based electrode materials have become highly significant for developing supercapacitor technology, which has attracted considerable attention in energy storage systems. Here, nitrogen-doped reduced graphene oxide (N-rGO) – Polyaniline (PANI) nanocomposites were synthesized by a facile two-step method in which in situ polymerization of aniline monomer was performed on hydrothermally synthesized N-rGO nanosheets in DBSA and H_2SO_4 medium for co-doping of PANI chains. The effects of various acid concentrations (DBSA:H_2SO_4 0.5 – 0.25:1 n/n) and N-rGO:aniline ratios (N-rGO:aniline 1:4–10 m/m) used in the preparation of the electrode material on the capacitive properties were investigated. It is found that the co-doped N-rGO-PANI nanocomposites exhibit a high specific capacitance of 346.3 F g^{-1} at 1 A g^{-1}, remarkable rate capacity (99.9%, 1–10 A g^{-1}) and excellent cycle stability at 5 A g^{-1} (81.3%, 5000 cycles) in a two-electrode system. As a result, constructing co-doped PANI chains and N-doped rGO provided a viable and simple way to improve the capacitive performances of supercapacitors.

Keywords Polyaniline · Graphene · Supercapacitor · Nitrogen doping · Nanocomposite

1 Introduction

Supercapacitors, which are new generation energy storage systems, have been gaining importance due to the increasing world population and the demand for energy [1]. Supercapacitors are regarded as a good alternative between batteries and fuel cells, owing to their superior properties, such as, high power density and long cycle life. In the fabrication of supercapacitors, development of low-cost electrode materials with high specific capacitance and high energy density, while maintaining their power density and long cycle life is still a necessity [2, 3].

Electrical double-layer capacitors (EDLC) and pseudocapacitors are two types of supercapacitors. While EDLC capacitors store energy electrostatically, pseudocapacitors store energy by faradaic redox reactions [4]. Carbon-based nanomaterials, such as, activated carbon, graphene, and carbon nanotubes with high surface area and high conductivity are used in EDLCs, but these capacitors have limited energy density. In pseudocapacitors, conductive polymers, metal oxides/hydroxides with high energy density and high theoretical capacitance are used. However, these structures have very low conductivity compared to carbon-based materials, which limits their specific capacitance related to their theoretical capacitance and rate capability. One approach to increase the electrochemical performance of supercapacitors is to prepare nanocomposites of EDLC and pseudocapacitor materials. In this way, it is aimed to produce electrode materials with high capacitance, high conductivity, high energy density, and surface area [5, 6].

Polyaniline (PANI) is one of the most commonly used conductive polymers in supercapacitors, with its high conductivity [7], high theoretical capacitance, abundant

✉ Nuray Yıldız
nyildiz@eng.ankara.edu.tr

1 Department of Chemical Engineering, Faculty of Engineering, Ankara University, 06100 Ankara, Türkiye, Turkey

2 Department of Chemical Engineering, Faculty of Engineering, İzmir Institute of Technology, 35430 İzmir, Türkiye, Turkey

3 Department of Chemical Engineering, Faculty of Engineering, Sivas Cumhuriyet University, 58140 Sivas, Türkiye, Turkey

4 Department of Chemical Engineering, Faculty of Engineering and Natural Sciences, Ankara Yıldırım Beyazıt University, 06010 Ankara, Türkiye, Turkey

availability, and low cost [8–10]. However, due to its low mechanical strength, PANI undergoes large volumetric changes during electrochemical characterizations and electrode stability is greatly reduced [11]. Hybridization of PANI with carbon nanostructures is a promising approach for production of high peformance electrode materials [12].

In the literature, there are essential studies in which polyaniline is used together with carbon nanostructures, such as, activated carbon, carbon nanotubes, graphene oxide (GO), reduced graphene oxide (rGO), etc. Wang et al. [13] prepared polyaniline film on graphene paper by in situ anodic electropolymerization and they determined that the specific capacitance of the material is 235 F g^{-1}. Meng et al.[14] combined polyaniline nanowires with 3D graphene and achieved a capacitance of 385 F g^{-1} at 0.5 A g^{-1}. Ahmed et al. [15], synthesized an electrode material by combining magnetic graphene and polyaniline at high temperature (900 °C) and reported a specific capacitance of 253 F g^{-1} at 5 mV s^{-1} with capacitive retention of 99% after 9000 cycles. Jin et al. [16] showed that rGO-PANI composite had a capacitance of 324.4 F g^{-1} at 1 A g^{-1}. Ahirrao et al. [4] used polyaniline coated with carbon cloth as the electrode material and reported a specific capacitance of 691 F g^{-1} at 1 A g^{-1}, which is a higher capacitance value compared to pure polyaniline and still retained 94% of its initial capacitance after 2000 cycles. Ji et al. [17] fabricated rGO-PANI composite with bio-inspired photo-/colloidal-lithography technique and obtained a capacitance value of 614 F g^{-1} at 1 A g^{-1} with capacitive retention of 85% after 10,000 cycles. Ajay et al. [18] manufactured an electrode material by combining activated carbon obtained from orange peels with polyaniline and reached a capacitance of 427 F g^{-1}at 2 mV s^{-1} with capacitive retention of 75% after 5000 cycles.

Among carbon-based nanomaterials, heteroatom doped reduced graphene oxide is a preferred material in supercapacitor applications due to its high conductivity and pseudocapacitance contrubition in addition to its EDL capacitance. Nitrogen doped reduced graphene oxide has drawn a great deal of attention because of its ease of production under mild conditions. N doping of graphene nanosheets introduces pyrrolic, pyridinic, and graphitic N bonds, which provide higher conductivity, higher wettability with aqueous electrolytes, and better electrochemical performance [19].

Recently, studies on nitrogen-doped reduced graphene oxide and polyaniline have attracted much interest. Liu et al. [20] synthesized N-rGO-PANI composites with using MnO_2 as the oxidizer and obtained a capacitance of 282 F g^{-1} at 1 A g^{-1}. Liu et al. [21] reduced GO with hydrazine and doped rGO with nitrogen using $NH_3.H_2O$. Then, they combined the N-rGO structure with polyaniline, resulting in a capacitance of 510 F g^{-1} at 1 A g^{-1} with capacitive retention of 74% after 2000 cycles.

To achieve enhanced specific capacitance and stability, co-doping of PANI with organic and incorganic acids is a recent approach. In co-doping process organic acids, such as, dodecylbenzene sulfonic acid (DBSA), p-toluene sulfonic acid (p-TSA) etc., provide improved electrochemical stability, processability, and better wettability with aquoues solutions, which leads to better interaction of polymeric structure with electrolyte ions and also graphene nanosheets to enhance the morphological and electrochemical properties of the nanocomposite. Furthermore, using inorganic acids like HCl, H_2SO_4, HNO_3 etc. with organic acids during co-doping process, maintains the conductivity of the polymer chains. Cho et al.[22] used camphorsulfonic acid as doping acid in the synthesis of PANI and the polymer showed a capacitance of 361 F g^{-1} at 0.25 A g^{-1}. Bilal et al.[23] used DBSA and H_2SO_4 as doping acids in the synthesis of PANI and showed that the capacitance of PANI reached 516 F g^{-1} at 0.5 A g^{-1}. Also, the electrode retained 57% of its capacitance after 1000 cycles. Das et al.[24] used benzene tetracarboxylic acids to dope the PANI structure and the polymer showed a capacitance of 107 F g^{-1}at 0.2 A g^{-1} with capacitive retention of 91% after 5000 cycles. Lakshimi et al. [25] used HCl as doping acid for the synthesis of PANI nanorod and obtained a capacitance of 106 F g^{-1} at 1 A g^{-1}.

In this study, N-rGO-PANI nanocomposites were fabricated with a facile, two-step method. In the first step, graphene oxide was reduced and doped with N atoms simultaneously by a simple hydrothermal method. In the second step, for the first time, in situ polymerization of aniline monomer was carried out on N-rGO nanosheets by using DBSA and H_2SO_4 for co-doping of PANI chains. The processable N-rGO-PANI nanofilms exhibited high electrochemical performance with high cyclic stability that proved to be a promising candidate for utilizing as a supercapacitor electrode material. N-rGO-PANI6 composite showed a specific capacitance of 346.30 F g^{-1} at 1 A g^{-1} with an excellent capacitive retention of 81.3% after 5000 cycles.

2 Materials and Methods

2.1 Materials

Graphite oxide was obtained from Grafen Chemical Industries (Turkey). Aniline (≥99.5%), sulfuric acid (H_2SO_4) (≥96%), DBSA (70% in isopropanol), ammonium persulphate (APS), Poly(vinylidene fluoride) (PVDF) and N-Methylpyrrolidone (NMP) were supplied from Sigma-Aldrich (Germany).

2.2 Preparation of N-rGO-PANI Nanocomposite

N-rGO-PANI nanocomposites were synthesized in two steps: N-rGO synthesis under hydrothermal conditions and in situ polymerization of aniline on the N-rGO surface. In the first step, graphite oxide (0.5 mg/mL) was added in water and sonicated in Elmasonic S 70 H, 150 W sonicator for 1 h. During this period, the graphene oxide layers separate from each other (0.34 nm to 0.75–0.822 nm) [26] under the effect of ultrasonication and GO structures form as layers. Then, 5 g urea was added in GO dispersion and the mixture was sealed in a Teflon lined 100 mL stainless steel autoclave and heated at 180 ºC for 12 h for sufficient N doping [27, 28]. The precipitated N-rGO nanosheets were washed with deionized (DI) water and dried at 60 ºC in vacuum.

In the second step, a homogeneous solution of 1.25 mg/mL of N-rGO was prepared in the ultrasonic bath and DBSA and H_2SO_4 were added at different rates (DBSA:H_2SO_4 $0.5-0.25$:1 n/n). The samples in which the N-rGO structure is used together with DBSA and H_2SO_4 are specified as N-rGO-PANI/DH, and the examples using only DBSA and H_2SO_4 are specified as N-rGO-PANI/D and N-rGO-PANI/H, respectively. Aniline monomer was added to the N-rGO-acid solution and stirred for 1 h at 4 °C. Then, APS solution (aniline:APS 1:1 n/n) was added dropwise to the solution containing N-rGO and stirred overnight 4 °C. After the termination of polymerization, ethanol was added to the solution to precipitate the resulting stable green dispersion. The precipitate obtained was washed 4 times with ethanol and 4 times with deionized water by centrifugation and then dried at 60 °C in vacuum. To determine the effect of the amount of aniline monomer on the electrochemical performance, syntheses were carried out using different mass ratios of N-rGO:aniline. The samples prepared with different N-rGO-aniline ratios was named as N-rGO-PANI4 (N-rGO:aniline 1–4 m/m), N-rGO-PANI6 (N-rGO:aniline 1–6 m/m), N-rGO-PANI8 (N-rGO:aniline 1–8 m/m) and N-rGO-PANI10 (N-rGO:aniline 1–10 m /m).

2.3 Characterizations

The structural characterizations of the samples were carried out with Fourier transform infrared (FT-IR) between 600 and 4000 cm^{-1} (Shimadzu FTIR 8400-S FTIR), Ultraviolet-visible spectroscopy between 200 and 1100 nm (Shimadzu 1601 UV–Vis spectrophotometer). The crystal structures of the samples were investigated with X-ray diffraction (XRD). XRD patterns were obtained with a Rigaku Ultima-IV powder XRD with CuKα radiation in a 2Θ range from 5 to 100°. The elemental composition of the samples was determined by PHI 5000 VersaProbe X-Ray Photoelectron Spectroscopy (XPS) with a binding energy range of 200–700 eV. The surface and morphological characterization of the samples were performed with a field-emission scanning electron microscopy (SEM) (FEI QUANTA 400 F) in which aqueous dispersions of samples were dropped on stubs coated with Al foil, and high-resolution transmission electron microscopy (HRTEM) (Jem Jeol 2100 F 200 kV HRTEM).

2.4 Electrochemical Measurements

The electrochemical performance of the prepared samples were investigated with utilizing a two-electrode configuration. Electrochemical measurements were carried out with a Gamry Reference 3000 potentiostat/galvanostat electrochemical workstation by performing galvanostatic charge/discharge (GCD), cyclic voltammetry (CV), and electrochemical impedance spectroscopy (EIS) analyses. The working electrodes were produced via coating of stainless steel (SS) current collectors with homogenous slurry of N-rGO-PANI nanocomposite (80%) with carbon black (15 wt%) and PVDF (5 wt%) in NMP. The prepared electrodes were dried in a vacuum oven at 70 °C for 24 h.

Electrochemical measurements in two-electrode configuration were carried out using a coin cell (Hohsen, HS Test Cell). 1 M H_2SO_4 was used as the electrolyte in the measurements. CV measurements were carried out in the potential window (-0.2–0.8 V) and the range of 5–200 mV/s scanning rates. EIS tests were performed in the frequency range of 0.01 Hz – 100 kHz with 10 points/decade at 0 V DC voltage and presented as Nyquist plots. Various current densities (1–10 A g^{-1}) were applied in the working potential ranges specified for the GCD measurements. Specific capacitance of the electrodes can be calculated from GCD analysis with Eq. (1).

$$C = \frac{2I\Delta t}{m\Delta V} \tag{1}$$

where, C (F g^{-1}) is the specific capacitance, I (A) is the response current, m (g) is the mass of the electrode, t (s) is the discharge time, and ΔV is potential window [29].

The energy and power density of two electrode cells were determined with Eqs. (2) and (3).

$$E = \frac{1}{2 \times 4 \times 3.6} CV^2 \tag{2}$$

$$P = \frac{3600E}{\Delta t} \tag{3}$$

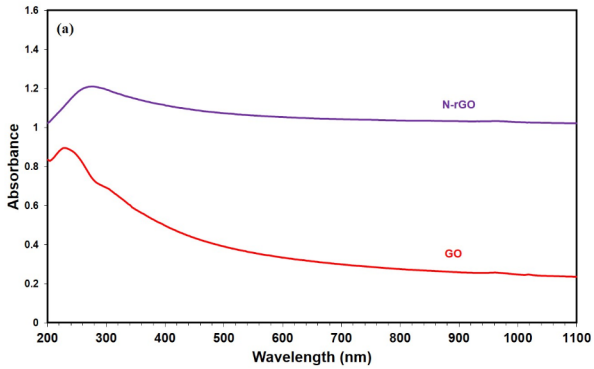

Fig. 1 UV-visible spectra of GO and N-rGO

where, E (Wh kg^{-1}) is the energy density, P (W kg^{-1}) is the power density, C (F g^{-1}) is the specific capacitance, V ise the potential range and, Δt (s) is the discharge time.

3 Result and Discussion

3.1 Characterization of the Composites

Figure 1 shows UV-visible spectra of GO and N-rGO, respectively. In the UV-visible spectrum of the N-rGO sample, the π→π* transition peak of GO structure at 230 nm is significantly shifted to the right (~276 nm) and the n→π* transitions of the C=O bonds at 300 nm was observed to be lost due to the effective removal of oxygenated functional groups in GO nanosheets. Figure 2 shows the XPS survey and C1s of GO. As seen in the survey spectrum, O1s peaks have high intensity due to the presence of oxygenated functional groups on the GO surface. C1s of GO was deconvoluted into C-C at 283.9 eV, C-O at 285.8 eV, C-O-C at 287.4 eV, and C=O at 288.3 eV [30]. Survey, C1s, N1s, and O1s spectra of N-rGO is given in Fig. 3. In the survey spectrum of the N-rGO sample, because of the reduction process with urea in hydrothermal conditions, the intensity of the C1s peaks increased, while the intensity of the O1s peaks decreased significantly due to effective deoxygenation and restoration of the sp^2 network of graphene nanosheets. From XPS survey spectra, the C/O atomic ratio in the N-rGO sample was determined as 13.84, and the C/O ratio in the GO sample was determined as 2.24. It proves that the oxygenated functional groups were effectively removed from GO. In addition, the reaction with urea in the hydrothermal condition caused the formation of N1s peaks around ~400 eV. In general, the doping of N atoms in graphene layers is examined in three basic classes: pyridinic, pyrrolic, and quaternary-N. Deconvolution of C1s spectrum of N-rGO sample resulted in C–C/C=C in the aromatic rings at 283.1 eV, C–O of epoxy at 284.5 eV, C-N at 286.2 eV, C=O at 289.3 eV, and O–C=O at 293.4 eV [31]. Intensity of C–C/C=C peak is the highest among other components, indicating successful removal of oxygen containing functional groups in GO [31, 32]. Additionally, low intensity of O–C=O peak shows that the sample is reduced effectively. Furthermore, presence of C-N peak shows that nitrogen was incorporated into the graphitic layer of GO [31]. N1s spectrum of N-rGO revealed pyridinic-N at 397.8 eV, pyrrolic-N at 398.9 eV, quaternary-N at 403.2 eV [32]. O1s spectrum exhibited C=O and C-O bonds at 531.7 and 529.6 eV, respectively [33]. XPS survey, C1s, N1s, and O1s spectra of N-rGO-PANI6 sample is shown in Fig. 4. C/O atomic ratio of N-rGO-PANI6 sample is 5.4 which is lower than that of N-rGO sample. This phenomenon is because of the addition of PANI into the structure of the nanocomposite, which was doped with oxygen-rich H_2SO_4 and DBSA. Deconvolution of C1s spectrum of N-rGO-PANI6 sample revealed five peaks; C–C/C=C in the aromatic rings at 283.4 eV, C–O of epoxy at 284.6 eV, C-N at 287.5 eV, C=O at 288.6 eV, and O–C=O at 289.4 eV [31]. High resolution spectrum of N1s was deconvoluted into five peaks; aromatic N-imines at 397.8 eV, pyridinic-N at 398.2 eV, pyrrolic-N at 399.2 eV, quaternary-N at 400.3 eV, and oxidized-N at 402.0 eV [32]. Aromatic N-imines peak originates from PANI and pyridinic, pyrrolic, and quaternary-N come from nitrogen atoms doped various sites of the graphitic layer [32]. O1s spectrum

Fig. 2 **a** Survey spectrum **b** C1s spectrum of GO

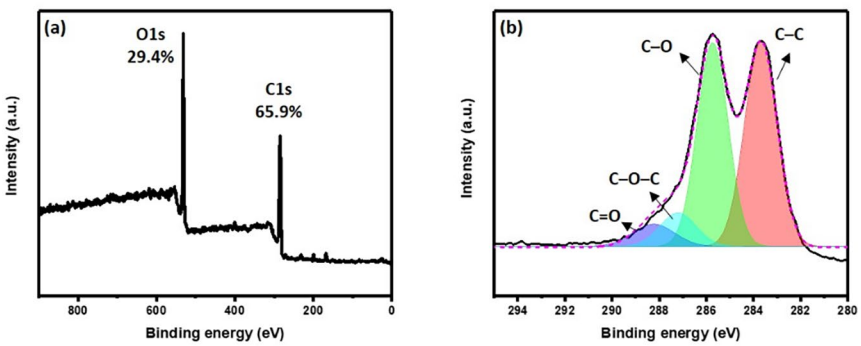

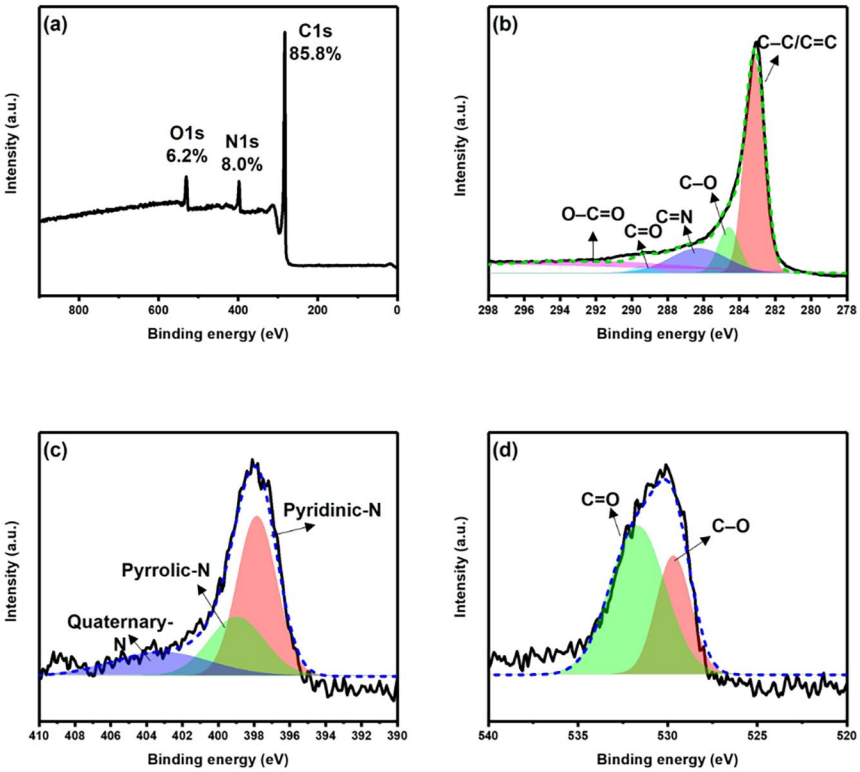

Fig. 3 **a** Survey **b** C1s **c** N1s **d** O1s spectra of N-rGO

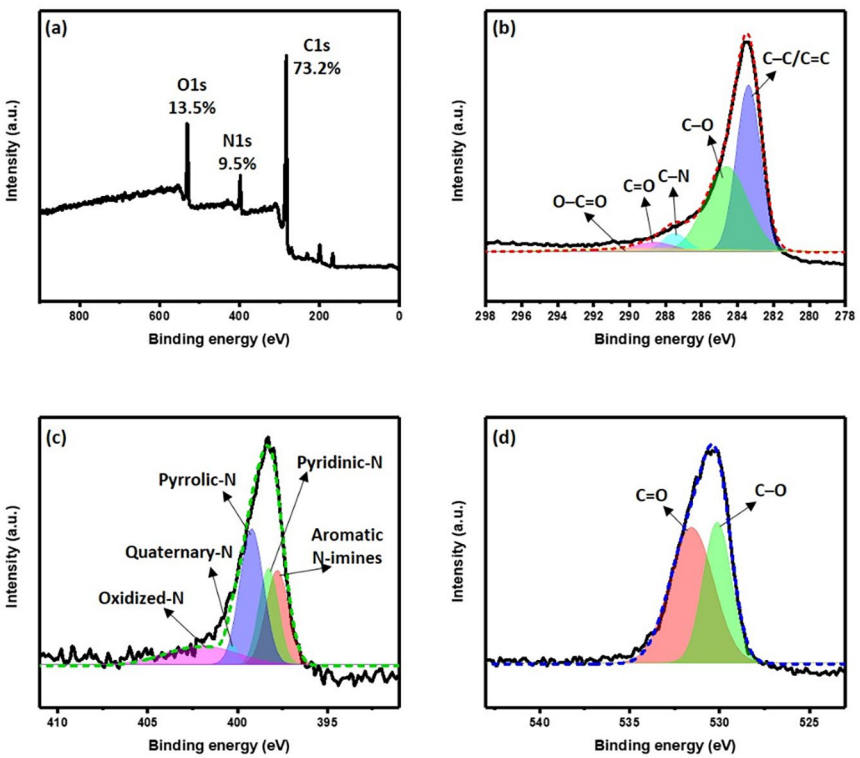

Fig. 4 **a** Survey **b** C1s **c** N1s **d** O1s spectra of N-rGO-PANI6

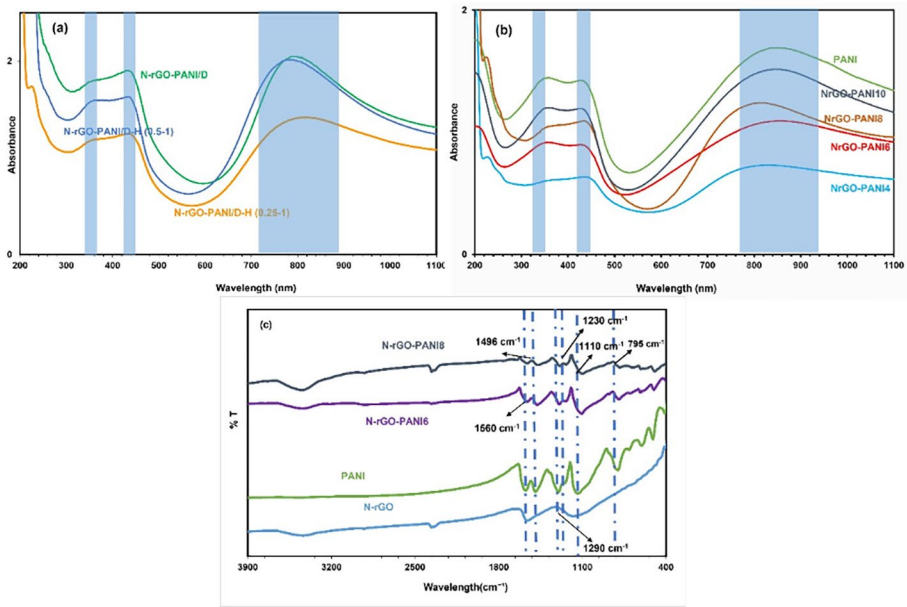

Fig. 5 **a** UV visible spectra of **a** N-rGO-PANI/D (0.5 M DBSA, N-rGO:aniline 1–8 m/m), N-rGO-PANI/D-H (0.5-1) (DBSA:H_2SO_4 0.5:1 n/n, N-rGO:aniline 1–8 m/m), N-rGO-PANI/D-H (0.25-1) (DBSA:H_2SO_4 0.25:1 n/n, N-rGO:aniline 1–8 m/m) **b** PANI (DBSA:H_2SO_4 0.25:1 n/n) and N-rGO-PANI (DBSA:H_2SO_4 0.25:1 n/n, N-rGO:aniline 1:4–10 m/m) **c** FTIR spectra of N-rGO, PANI/D-H (0.25-1) (DBSA:H_2SO_4 0.25:1 n/n, N-rGO:aniline 1–8 m/m), N-rGO-PANI6 and N-rGO-PANI8

of N-rGO-PANI indicates presence of C = O and C-O bonds at 531.5 and 530.1 eV, respectively [33]. With XPS analysis, it was determined that the reduced graphene oxide layers were successfully doped with N atom as a result of the reaction with urea under hydrothermal conditions. Especially in supercapacitor applications, the presence of pyrrolic and pyridinic-N can store energy with the pseudocapacitance mechanism, and graphitic-N can significantly increase the conductivity of the layers, shows that the graphene layers are successfully doped with N in the hydrothermal condition in the presence of urea. Moreover, PANI coating of N-rGO was observed in N1s spectrum of N-rGO-PANI sample with the emergence of aromatic N-imines.

UV-visible spectra of N-rGO-PANI/D (0.5 M DBSA, N-rGO:aniline 1–8 m/m), N-rGO-PANI/DH (0.5-1) (DBSA:H_2SO_4 0.5:1 n/n, N-rGO:aniline 1–8 m/m) and N-rGO-PANI/DH (0.25-1) (DBSA:H_2SO_4 0.25:1 n/n, N-rGO: aniline 1–8 m/m) composites are shown in Fig. 5a. For PANI and N-rGO-PANI nanocomposite produced with different molar ratios (DBSA/H_2SO_4) of doping acids samples, shoulder-shaped peak between 340 and 360 nm wavelength caused by $\pi \rightarrow \pi^*$ electron transitions of PANI, the band between 400 and 440 nm wavelengths associated with the protonation step of PANI chains, and the sharp peak between 780 and 850 nm wavelengths due to the presence of polarons, formed because of the doping process in the UV visible spectrum of each sample. In UV-visible spectra of nanocomposites, the band at approximately 280 nm due to the $\pi \rightarrow \pi^*$ transition of N-rGO nanolayers is not seen expectedly, due to the N-rGO surface being completely covered with the PANI.

N-rGO-PANI (DBSA: H_2SO_4 0.25:1 n/n, N-rGO:aniline 1:4–10 m) prepared using PANI (DBSA:H_2SO_4 0.25:1 n/n) and different aniline amounts in samples are shown in the UV-visible spectrum (Fig. 5b). Similarly, it was found that all three characteristic peaks belonging to PANI were seen in the UV-visible region spectrum of the samples. However, in parallel with the increase in the amount of monomer used during the synthesis, the intensity of the characteristic bands of PANI in the UV-visible spectrum of the N-rGO-PANI samples also increased, which may be attributed to thickening of the polymeric layer prepared on N-rGO nanosheets. As a result, PANI synthesis was successfully carried out on the surface of N-rGO nanolayers in the presence of DBSA and/or H_2SO_4.

Figure 5c shows, FTIR spectra of N-rGO, PANI (DBSA:H_2SO_4 0.25:1 n/n), N-rGO-PANI6 and N-rGO-PANI8 composites. FTIR spectra of N-rGO-PANI nanocomposites revealed all characteristic peaks belonging to the PANI structure. Additionally, the peak indicating quinone ring deformation of PANI shifted from 1573 cm^{-1} to 1560 cm^{-1}, the peak due to benzoid ring deformation shifted from 1470 cm^{-1} to 1496 cm^{-1}, CN tensile vibration shifted from 1303 cm^{-1} to 1290 cm^{-1}, C-N^+ tensile vibration shifted from 1242 cm^{-1} to 1230 cm^{-1}, -NH^+ tensile vibration shifted from 1125 cm^{-1} to 1110 cm^{-1} and, out-of-plane bending vibration of CH bond shifted from 802 cm^{-1} to 795 cm^{-1}. These findings indicate the strong interaction between N-rGO and PANI, which is crucial for obtaining high electrochemical performance. Moreover, PANI synthesis proceeds on many nucleation centers of the N-rGO surface and is successfully synthesized.

Figure 6a shows the XRD patterns of GO and N-rGO samples. The sharp peak with a center of 10.74° in the GO diffraction pattern indicates the planar reflection (002) structure of the GO layers. At the same time, this characteristic

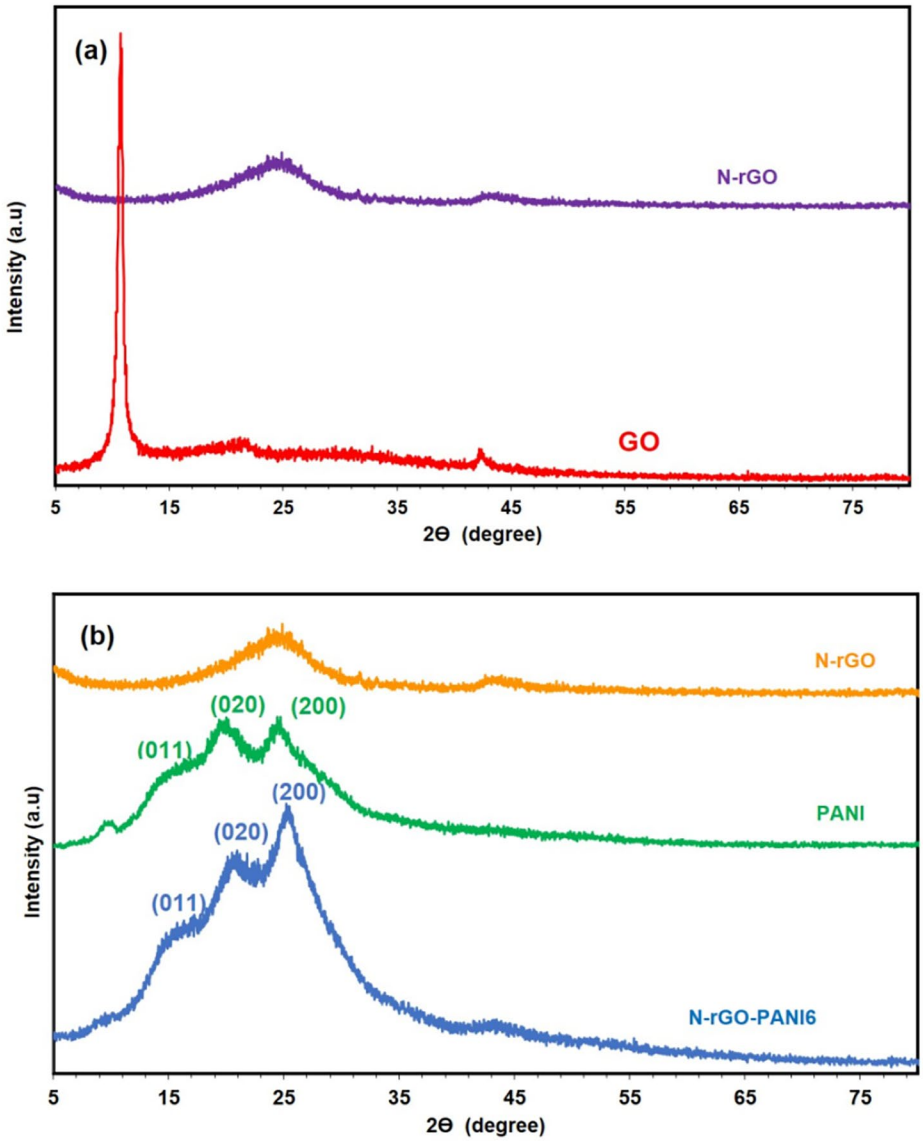

Fig. 6 **a** XRD patterns of GO and N-rGO **b** PANI (DBSA:H_2SO_4 0.25:1 n/n) and N-rGO-PANI6 (DBSA:H_2SO_4 0.25:1 n/n, N-rGO:anilin 1:6 m/m)

peak of the GO structure shows that the distance (d-spacing) between the graphene layers is 0.822 nm. The entry of water molecules between the layers of graphite and the oxidation of graphite and the formation of oxygenated functional groups on the layers during the GO production process show that the distance between the layers in the GO structure increases compared to the perfect graphite structure [34–36]. Because of the effective chemical reduction of GO by the hydrothermal method, it was observed that the (002) crystal diffraction pattern of GO disappeared completely and a broad peak was formed at $2\Theta = 25.2°$ in Fig. 6a. This new peak indicates that the d-spacing value for N-rGO nanolayers is 0.36 nm [37]. The decrease in the distance between the graphene layers and the disappearance of the peak belonging to GO under hydrothermal conditions indicates that the oxygenated functional groups are significantly removed. Figure 6b shows XRD patterns of the PANI, and N-rGO-PANI6 samples. Three characteristic peaks corresponding to the crystal planes (001), (020) and, (200) of the PANI (0.25-1) sample synthesized in 0.1 M H_2SO_4 and 0.05 M DBSA medium overlap with the diffraction pattern of the N-rGO-PANI6 nanocomposite. PANI polymeric structures with crystalline properties were successfully produced by in situ polymerization of aniline monomer on the N-rGO surface.

Figure 7 shows TGA curves of PANI (DBSA: H_2SO_4 0.25:1 n/n) and N-rGO-PANI6 (DBSA:H_2SO_4 0.25:1 n/n, N-rGO:aniline 1:6 m/m) samples. Both PANI and N-rGO-PANI (1–6) samples exhibited three main weight loss steps. The first weight loss of the samples, occurred because of the removal of moisture at a temperature of about 100 °C. The second weight loss, occurred due to the degradation of

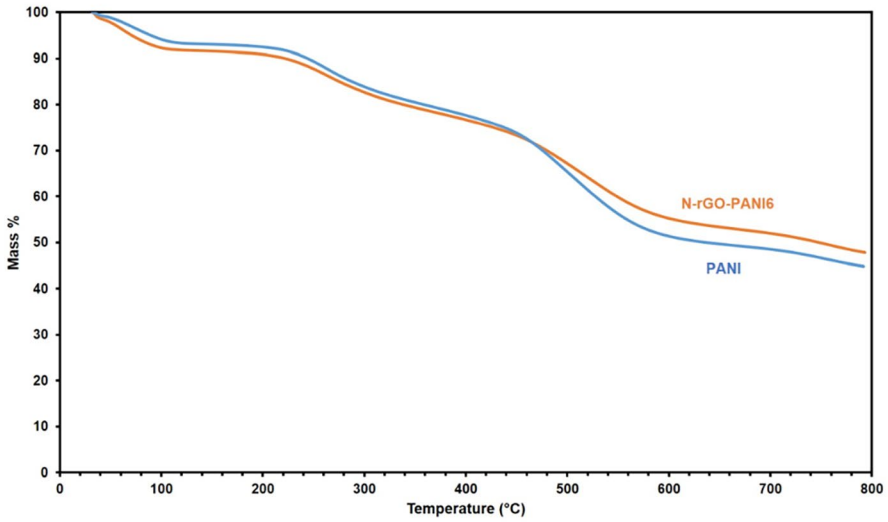

Fig. 7 TGA curves of PANI (DBSA:H_2SO_4 0.25:1 n/n) and N-rGO-PANI6 (DBSA:H_2SO_4 0.25:1 n/n, N-rGO:anilin 1:6 m/m)

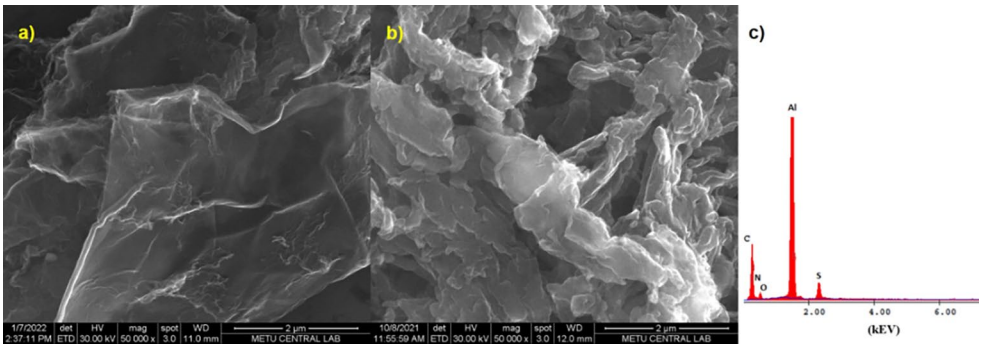

Fig. 8 **a** SEM image of N-rGO **b** SEM image of PANI (DBSA:H_2SO_4 0.25:1 n/n) **c** EDX specrtum of PANI (DBSA:H_2SO_4 0.25:1 n/n)

H_2SO_4 and DBSA molecules in the temperature range of 215–430 °C. Finally, since the skeletal structure of PANI started to degrade at approximately 450–550 °C, considerable weight loss occurred in the samples [38, 39]. Since the analyses were carried out in a nitrogen atmosphere, the carbonization of the polymer did not occur and when the analysis temperature reached 800 °C, the total weight loss percentages of PANI and N-rGO-PANI samples were 55.2% and 52.2%, respectively. This is an indication that the prepared nanocomposite structure has high thermal stability.

SEM images of N-rGO and PANI (DBSA:H_2SO_4 0.25:1 n/n) are given in Fig. 8. SEM images demonstrate that the N-rGO layers with thin and curved edges (Fig. 8a) are covered by the PANI polymeric structure (Fig. 8b). Additionally, it is observed that the morphological structure of polyaniline synthesized by polymerization on the N-rGO surface is different from the structure of pure polyaniline synthesized directly in the solvent medium. While pure polyaniline consists of interconnected forms of rod-like structures in micron scale, polyaniline prepared by in situ polymerization in the presence of N-rGO encased the 2-D surface in thin layers. EDX spectrum of PANI (DBSA:H_2SO_4 0.25:1 n/n) exhibited C, N, O, and S atoms elements (Fig. 8c) in accordance with XPS results. SEM images of N-rGO-PANI4, N-rGO-PANI6, N-rGO-PANI8, and N-rGO-PANI10 are given in Fig. 9. It can be seen that coating thickness of these polymeric layers on N-rGO increases with the amount of aniline monomer used. EDX spectrum of N-rGO-PANI6 given in Fig. 9f shows considerable amount of S atoms in the nanocomposite corresponding to the presence of DBSA and H_2SO_4 molecules in the nanocomposite structure, which also confirm TGA results. DBSA is an effective surfactant that also undertakes the co-dopant role, responsible for preventing further growth and agglomeration of polymeric structures for the production of nanocomposite films. Moreover, DBSA increases the interaction of nanocomposite with aqueous solutions to bring processability and wettability with aqueous electrolytes. The adjustable morphological structure is very advantageous for supercapacitor applications, as the electrolyte diffusion distance can be lowered by adjusting the coating thickness controlled by the aniline/N-rGO m/m ratio. The strong interaction between N-rGO and PANI components were determined by FTIR spectrum and XRD analysis, which was also confirmed by SEM images. Figure 10 shows the elemental mapping images of N-rGO-PANI6 sample. C, O, N, and S elements

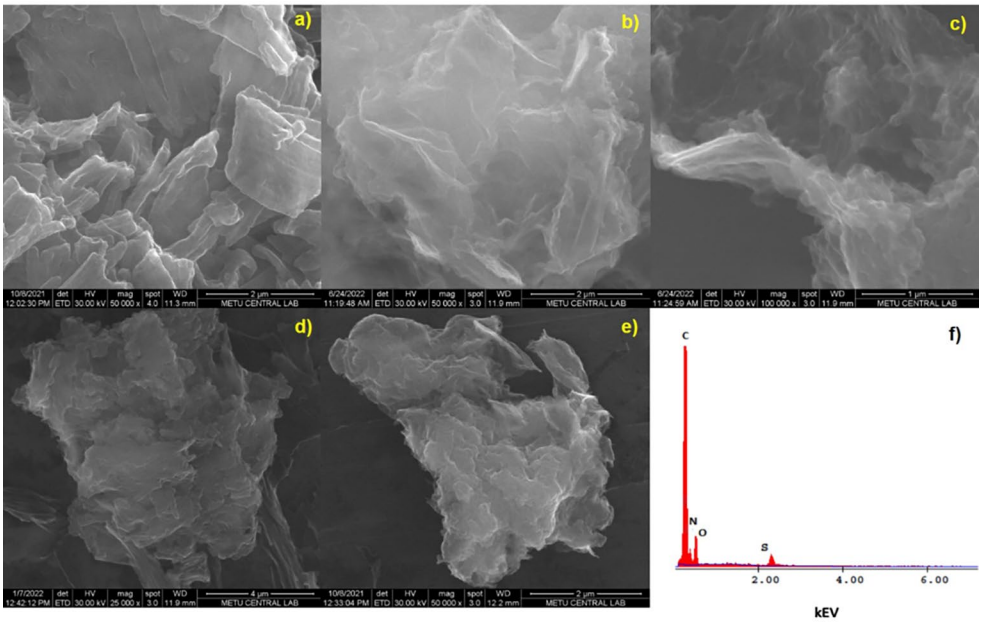

Fig. 9 **a** SEM images of **a** N-rGO-PANI4 **b** N-rGO-PANI6 **c** N-rGO-PANI6 **d** N-rGO-PANI8 **e** N-rGO-PANI10 **f** EDX spectrum of N-rGO-PANI6

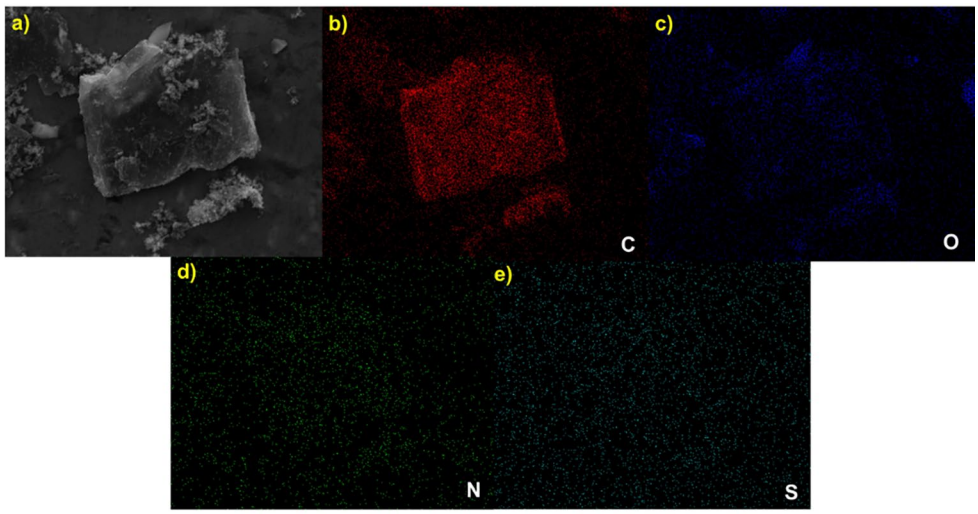

Fig. 10 **a** SEM image of N-rGO-PANI6 **b** elemental mapping of C **c** elemental mapping of O **d** elemental mapping of N

were homogeneously distributed throughout the nanocomposite, indicating an excellent interaction between N-rGO and PANI during the polymerization process [40].

TEM images of N-rGO and N-rGO-PANI6 samples are shown in Fig. 11. N-rGO displays a 2-D sheet-like structure with micro-wrinkles [41]. SAED pattern of N-rGO suggests the formation of a crystalline structured material (Fig. 11a inset) [42, 43]. In Fig. 11b and c consistent with the SEM images, it was observed that the N-rGO surface was homogeneously coated with the polymers and N-rGO-PANI ultrathin films were successfully produced. SAED pattern of N-rGO-PANI6 (Fig. 11c inset) reveals the polycrystalline structure of the nanocomposite in accordance with the XRD result [20, 44, 45].

3.2 Electrochemical characterization

CV curves of the synthesized DBSA doped N-rGO-PANI/D, H_2SO_4 doped N-rGO-PANI/H, DBSA and H_2SO_4 co-doped N-rGO-PANI/DH, and DBSA and H_2SO_4 co-doped PANI samples in two-electrode configuration at 20 mV/s scanning rate are given in Fig. 12a. It was observed that the characteristic two redox transitions of PANI were prominent. The redox peak at about 0.2 V indicates leucoemeraldine/emeraldine transformation. The redox couple at about 0.5 V correspond to emeraldine/pernigraniline transition [23, 46]. The peaks in the N-rGO-PANI/D-H (0.25-1) electrode were more prominent than those in the N-rGO-PANI/D, N-rGO-PANI/H, N-rGO-PANI/D-H (0.5-1) and PANI (DBSA:H_2SO_4 0.25:1 n/n) electrodes. This is because H_2SO_4 reduces the ion transfer resistance of the composite

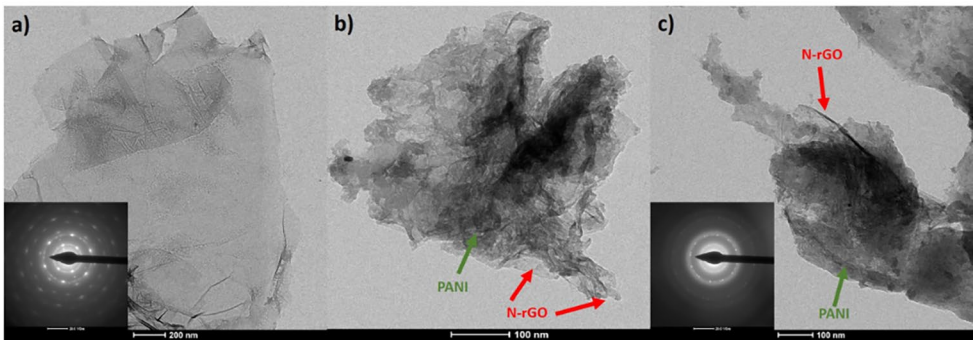

Fig. 11 TEM images of **a** N-rGO (inset is SAED pattern) **b** and **c** N-rGO-PANI6 (inset is SAED pattern)

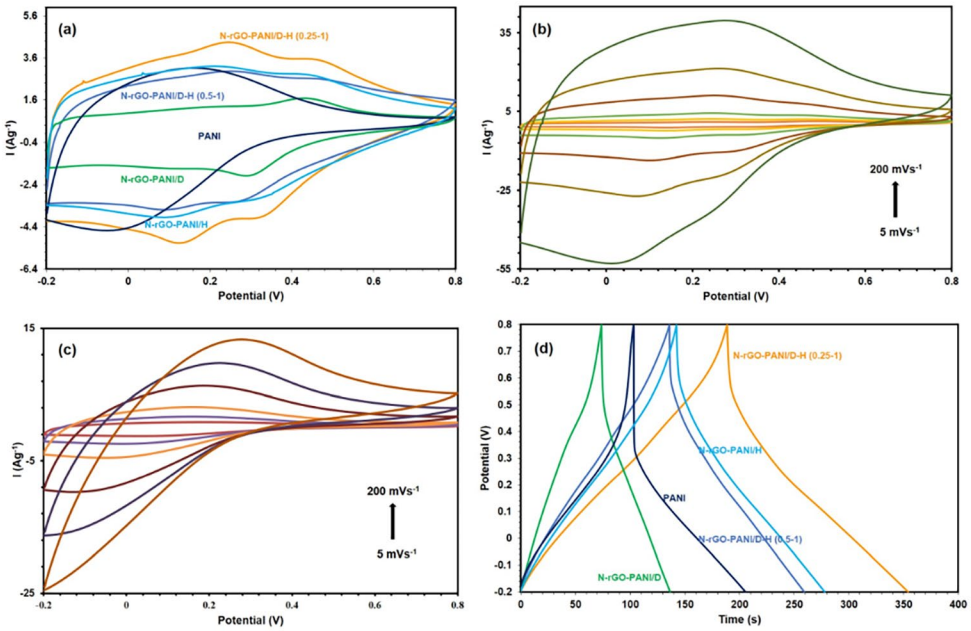

Fig. 12 CV curves of PANI (DBSA:H_2SO_4 0.25:1 n/n), N-rGO-PANI/D, N-rGO-PANI/DH (0.5-1), N-rGO-PANI/DH (0.25-1) and N-rGO-PANI/H electrodes at 20 mV s^{-1}, **b** CV curves of N-rGO-PANI/DH (0.25-1) electrodes at 5-200 mV s^{-1}, **c** CV curves of PANI (DBSA:H_2SO_4 0.25:1 n/n) electrodes at 5-200 mV s^{-1}, **d** GCD curves of PANI (DBSA:H_2SO_4 0.25:1 n/n), N-rGO-PANI/D, N-rGO-PANI/DH (0.5-1), N-rGO-PANI/DH (0.25-1) and N-rGO-PANI/H electrodes at 1 A g^{-1}

and increases its conductivity, while DBSA improves the surface properties of the material. It has been determined that the best concentrations where both doping acids can show their unique properties, are 0.25:1 ratio [23].

Having the higher CV area, co-doped N-rGO-PANI nanocomposite electrodes exhibit better capacitive properties, while DBSA doped N-rGO-PANI and H_2SO_4 doped N-rGO-PANI samples may suffer from their significantly lower conductivity compared to co-doped samples, Fig. 12b and c show the CV curves of N-rGO-PANI/DH (0.25-1) and PANI (DBSA: H_2SO_4 0.25:1 n/n) electrodes between 5 and 200 mV s^{-1} scan rates, respectively. As an ideal supercapacitor behavior, the response current values of the electrodes increase with increasing scanning rate in CV analysis. Also, the increase in scanning rate limits the access of electrolyte ions into the electrode material. At high scanning rates, only the surface portion of the electrode material is involved in the electrochemical process. Therefore, redox peaks that can be seen clearly at low scan rates may not be visible at high scan rates. The CV curves of the N-rGO-PANI structure (Fig. 12b) show that the composite is less affected by these restrictions compared to PANI (Fig. 12c). Micron-scale in pure PANI prevent the inner parts of the particles from participating to the electrochemical process, reduce performance and stability. PANI transition peaks, which cannot be seen at high scanning rates, indicate that the material has limited electrochemical performance. However, by coating the PANI structure on the N-rGO structure as a thin film, the ion diffusion length for ion transfer is shortened and the material is freed from structural constraints.

GCD curves of PANI (DBSA:H_2SO_4 0.25:1 n/n), N-rGO-PANI/D, N-rGO-PANI/H, N-rGO-PANI/DH (0.5-1) and N-rGO-PANI/DH (0.25-1) electrodes at 1 A g^{-1} current density are given in Fig. 12d. The capacitances of PANI, N-rGO-PANI/D, N-rGO-PANI/H, N-rGO-PANI/DH (0.5-1) and N-rGO-PANI/DH (0.25-1) samples are 282.1 F g^{-1}, 134.5 F g^{-1}, 283.13 F g^{-1}, 264.33 F g^{-1}, and 342.7 F g^{-1}, respectively. Because of the analyses performed at a current density of 1 A g^{-1}, the electrode with the best performance was determined as N-rGO-PANI/DH (0.25-1). Similarly with CV curves GCD analysis also displays, co-doped N-rGO-PANI/DH nanocomposite samples exhibit better

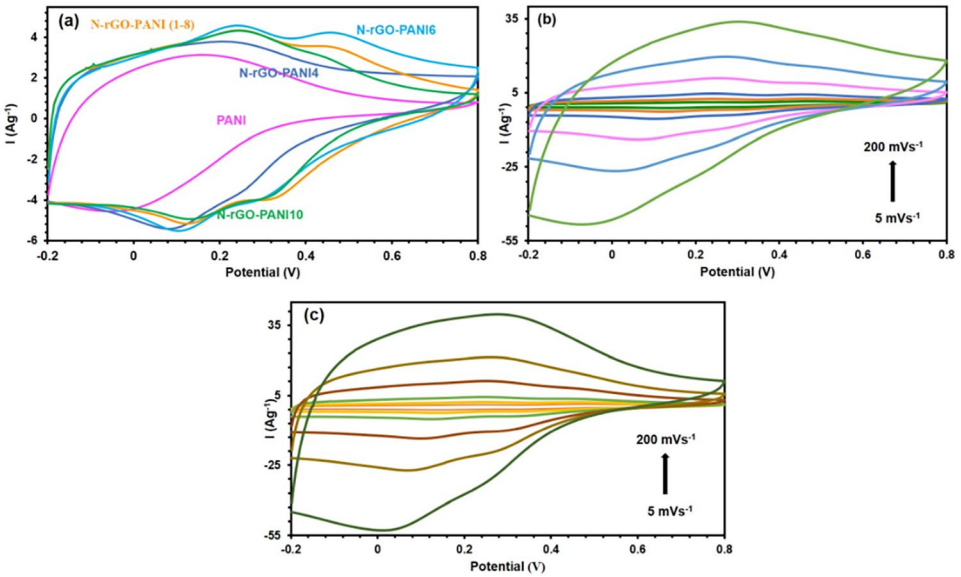

Fig. 13 CV curves of N-rGO-PANI (DBSA:H_2SO_4 0.25:1 n/n, N-rGO:anilin 1:4–10) samples at 20 mV s^{-1}, **b** CV curves of N-rGO-PANI6 at 5-200 mV s^{-1}, **c** CV curves of N-rGO-PANI8 at 5-200 mV s^{-1}

capacitive properties compared to pristine PANI and DBSA doped N-rGO-PANI/D electrodes. The enhanced specific capacitance of co-doped nanocomposites is because of their excellent surface properties and maintaining their high conductivity. The co-doping process may have provided formation of ultrathin stable nanocomposite 2-D networks having high electroactive surface area, low ion transfer distance, good wettability with electrolyte ions, and high conductivity. However, the increase in DBSA/H_2SO_4 molar ratio caused a decrease in the specific capacitance, which may be attributed to the presence of increased number of DBSA molecules having high interaction with the nanocomposite structure, consequently reducing electronic conductivity and ion transfer.

Subsequently, syntheses containing different ratios of N-rGO:aniline (1:4–10 m/m) were carried out to determine the effect of PANI coating the N-rGO nanosheets on the electrochemical performance of N-rGO-PANI samples. Figure 13a shows CV curves of N-rGO-PANI4, N-rGO-PANI6, N-rGO-PANI8, and N-rGO-PANI10 at 20 mV/s scan rate in -0.2-0.8 V potential range. Each nanocomposite display the redox transitions of PANI, while N-rGO-PANI6 and N-rGO-PANI8 electrodes display higher CV area, revealing their higher specific capacitance. CV curves of N-rGO-PANI6 and N-rGO-PANI8 samples with different scan rates are given in Fig. 13b and c. In both samples, an increase was observed in current density values with the increase in the scan rate, and no significant change was observed in the shapes of the CV curves, the redox transitions of PANI are still prominent at the highest applied scan rate, because of their high electrochemical stability and ion transfer properties.

GCD analysis was also carried out to examine the specific capacitance values of N-rGO-PANI electrodes produced with various aniline/N-rGO ratios. Figure 14a shows the GCD curves of N-rGO-PANI (DBSA:H_2SO_4 0.25:1 n/n, N-rGO:aniline 1:4–10) samples at 1 A g^{-1} current density between −0.2 and 0.8 V. The capacitance values of N-rGO-PANI4, N-rGO-PANI6, N-rGO-PANI8, and N-rGO-PANI10 electrodes at 1 A g^{-1} current density were calculated as 310 F g^{-1}, 346.3 F g^{-1}, 342.7 F g^{-1}, 325.6 F g^{-1}, respectively. Compared to pristine PANI (282.1 F g^{-1}, Fig. 12d), N-rGO-PANI nanocomposite samples exhibited higher specific capacitance values, because of uniform coating of PANI polymeric films on heteroatom doped, highly conductive N-rGO nanosheets. Additionally, the increase in aniline/N-rGO ratio between 1:4–1:8 resulted in enhencament of the specific capacitance, but further increase in the aniline amount (N-rGO-PANI10) led to a decrease in the capacitance because of the thickening of the PANI layer on the nanocomposite film, which is also responsible for the increase in the ion transfer distance. GCD curves of N-rGO-PANI6 and N-rGO-PANI8 electrodes between 1 and 10 A g^{-1} are shown in Fig. 14b and c. The capacitance values of N-rGO-PANI6 and N-rGO-PANI8 electrodes at 1 A g^{-1} to 10 A g^{-1} were determined as 346.3 F g^{-1} to 345.9 F g^{-1} (Fig. 14b), and 342.7 F g^{-1} to 342.2 F g^{-1} (Fig. 14c) with displaying excellent rate capability (99.9% and 99.8%, respectively) thank to its high conductivity, strong interaction with electrolyte ions and low ion transfer distance because of its ultrathin 2-D film structure.

The Nyquist plots of N-rGO-PANI4 N-rGO-PANI6, N-rGO-PANI8 and N-rGO-PANI10, are given in Fig. 15. The Nyquist plots consist of a semicircle in the high frequency region giving charge transfer resistance (R_{ct}), and

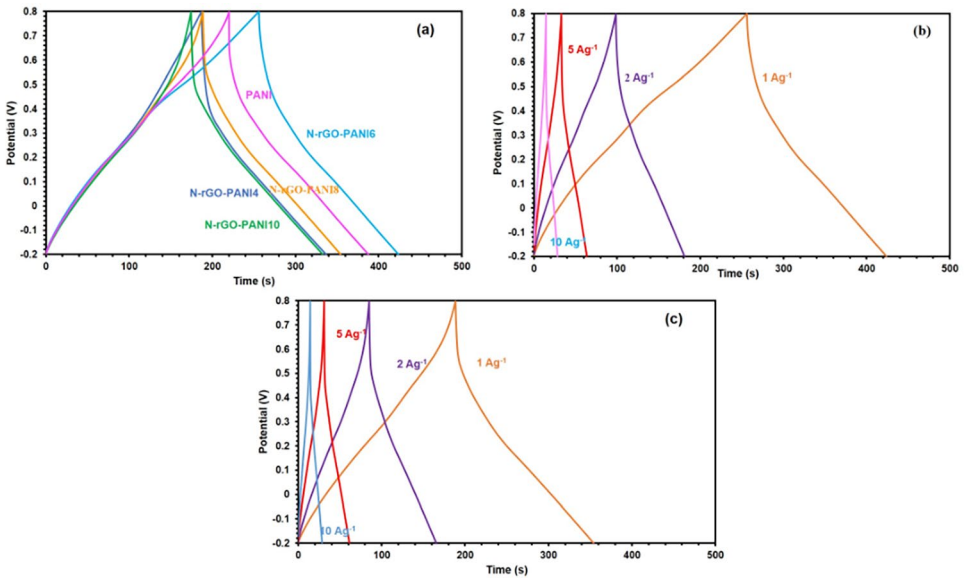

Fig. 14 GCD curves of N-rGO-PANI (DBSA:H_2SO_4 0.25:1 n/n, N-rGO:aniline 1:4–10) samples at 1 A g^{-1}, **b** GCD curves of N-rGO-PANI6 between 1 and 10 A g^{-1}, **c** GCD curves of N-rGO-PANI8 between 1 and 10 A g^{-1}

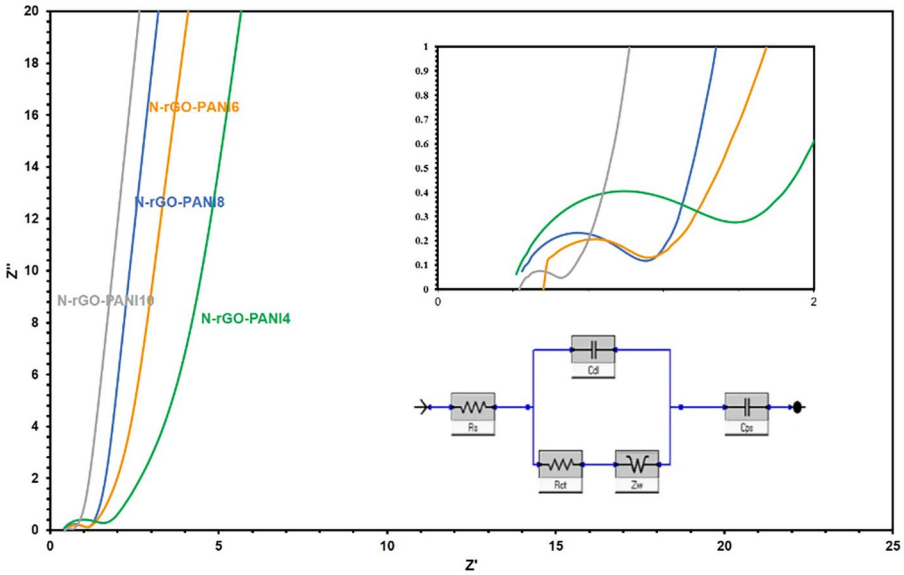

Fig. 15 Nyquist plots of PANI (DBSA:H_2SO_4 0.25:1 n/n), N-rGO-PANI (1–6) (DBSA:H_2SO_4 0.25:1 n/n, N-rGO:aniline 1:6) and samples N-rGO-PANI (1–8) (DBSA:H_2SO_4 0.25:1 n/n, N-rGO:aniline 1:8) samples

a straight line at the low frequency region related to the capacitive behaviour of the electrodes. The R_{ct} values of N-rGO-PANI4 N-rGO-PANI6, N-rGO-PANI8 and N-rGO-PANI10 were determined as 0.96 Ω, 0.6 Ω, 0.56 Ω and 0.19 Ω, respectively. Because of their excellent surface properties and high conductivity, N-rGO-PANI nanocomposites exhibited very low R_{ct} values. Additionally, the slope of the curve in the Nyquist plot of N-rGO-PANI electrodes in the low frequency region is an indication that their properties are close to the ideal capacitor.

Another important parameter for the applicability of the electrode material as a supercapacitor is the cycle stability. Among the N-rGO-PANI samples, the samples showing the highest electrochemical performance were determined as N-rGO-PANI6. Accordingly, the cycle stability of N-rGO-PANI6 was investigated, and the change in the capacitance of N-rGO-PANI6 electrode with the number of cycles are shown in Fig. 16a. N-rGO-PANI6 sample exhibited a specific capacitance of 346.1 F g^{-1} at a current density of 5 A g^{-1} and the sample exhibited 81.3% specific capacitance retention after 5000 cycles. Because of the excellent mechanical strength of N-rGO nanosheets and strong interaction between PANI film with N-rGO the nanocomposite electrodes exhibited high cyclic stability. This interaction limits continuous swelling-shirinking of PANI structures during the cycling process. Figure 16b shows the change in capacitanece of N-rGO-PANI6 electrode between 1 and 10 A g^{-1} after the 5000 cycles. As shown in the Fig. 16c

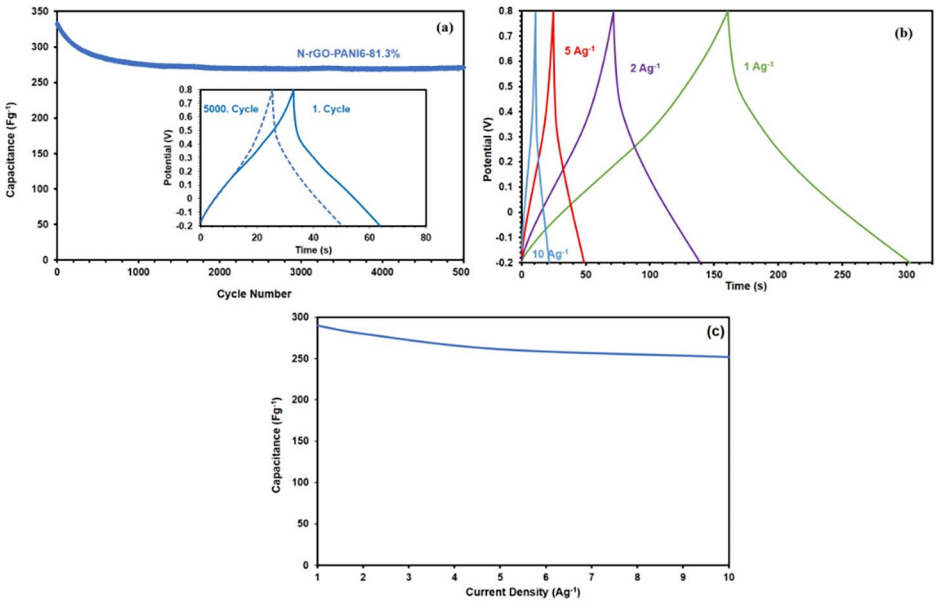

Fig. 16 Cycle stability of N-rGO-PANI6, **b** GCD curves of N-rGO-PANI6 between 1 and 10 A g^{-1} after 5000 cycle, **c** Capacitance of N-rGO-PANI6 with different current densities after 5000 cycle

Table 1 Comparison for the electrochemical properties of the N-rGO-PANI and the reported Graphene-PANI based electrodes

Study	Electrode	Doping Agent	Configuration	Specific Capacitance (1 A g^{-1}) (F g^{-1})	Specific Capacitance (10 A g^{-1}) (F g^{-1})	Capacitance Retention	Cyclic Stability
[47]	PANI	Camphorsulfonic acid (CSA)	Three-electrode	600.7	419.2	70%	74% 1000
[48]	PANI-Au	Dodecylbenzene sulfonic acid (DBSA)	Three-electrode	292.2 (0.5 A g^{-1})	173	60%	86% 3000
[49]	GO/Pt/DBSA/PANI	Dodecylbenzene sulfonic acid (DBSA)	Three-electrode	227	Not reported	Not reported	96% 1500
[23]	PANI	Dodecylbenzene sulfonic acid (DBSA), Sulfuric Acid	Three-electrode	516 (0.5 A g^{-1})	266 (25 A g^{-1})	51.5%	57% 1000
[50]	NCF-PANI	P-TSA (p-toluene sulfonic acid)	Three-electrode	139	97.3	70%	89% 5000
[51]	PANI	HCl-Phytic Acid	Three-electrode	350	315	90%	99% 500
[52]	SPANI/SrGO	Naphthalene Sulfonic Acid	Two-electrode	345.7	235.8 (5 A g^{-1})	68%	89% 2500
[53]	PANI	hyperbranched polyesters (HBPE)- Dodecyl hydrogen sulfate-Sulfiric Acid	Two-electrode	300 (0.2 A g^{-1})	Not reported	Not reported	75% 1500
This Work	N-rGO/PANI	Dodecylbenzene sulfonic acid (DBSA)-Sulfiric Acid	Two-electrode	346.3	345.9	99.9%	81.3% 5000

N-rGO-PANI6 sample exhibited a specific capacitance of 290 F g^{-1} at 1 A g^{-1} and 251.9 F g^{-1} at 10 A g^{-1}. It was determined that the electrode still exhibited high stability (81.3%) even after 5000 cycles.

The values of R_{ct}, the specific capacitances, the energy density and the power density of PANI, N-rGO-PANI4, N-rGO-PANI6, N-rGO-PANI8 and N-rGO-PANI10 are given in Table 1. The prepared composites showed good energy density compared to the aqueous electrolyte with limited operating voltage range. Since the potential range is determined as 1 V in all electrochemical analyses, the energy density varies directly with the capacitance. Also, the samples retained their energy density at high power density values. This is due to the high rate capability of the composites containing N-rGO.

Table 1 represents a comparison of the electrochemical performance of co-doped N-rGO-PANI nanocomposite with reported studies in the literature containing organic acids as dopants for PANI. The two-electrode configuration reflects more accurate results compared to the three-electrode

configuration because of the similar configuration and charge transfer mechanism similar to practical supercapacitors. The electrochemical measurements carried out in symmetrical two-electrode configuration exhibit N-rGO-PANI nanocomposites have high specific capacitance, high cyclic stability, and excellent rate capability. The in situ polymerization of aniline on highly conductive N-rGO nanosheets, which provides high surface area and plenty of active centers for polymerization, provided effective coating of N-rGO with polymeric structure. Moreover, co-doping of PANI with DBSA and H_2SO_4 ensured the formation of ultrafine polymeric films on N-rGO nanosheets, having high stability and wettability with electrolyte while maintaining its high conductivity.

4 Conclusions

In summary, co-doped conducting polymer based N-rGO-PANI was synthesized with a two-step green approach. Graphene oxide was reduced with urea under hydrothermal conditions and N-rGO was obtained by doping with nitrogen. N-rGO-PANI structure with high conductivity and short ion path was obtained by coating the N-rGO with aniline in the presence of DBSA and H_2SO_4. With the strong interactions between the graphene structure and the conductive polymer, it has been understood that the N-rGO-PANI, which performs both EDLC and pseudocapacitance, has high specific capacitance, excellent rate capability, and long cycle life. In the symmetric two-electrode configuration, 346.3 F g^{-1} capacitance was obtained at a current density of 1 A g^{-1} in the N-rGO-PANI composite. The N-rGO-PANI nanocomposite retained 81.3% of its initial specific capacitance after 5000 consecutive cycles at a current density of 5 A g^{-1}. Furthermore, a high energy density of 12.02 Wh kg^{-1} and high power density of 257.9 W kg^{-1} were obtained at 1 A g^{-1} for the cell with N-rGO-PANI6 nanocomposite. The co-doped PANI based carbon nanostructure nanocomposites are promising electrode materials for supercapacitor applications because of their high processability, unique surface properties with high specific capacitance, cycle life, and excellent rate capability.

Supplementary Information The online version contains supplementary material available at https://doi.org/10.1007/s10904-022-02456-0.

Acknowledgements The authors thank The Scientific and Technological Research Council of Türkiye (TÜBİTAK; Project No 120M752).

Author contributions All authors contributed to the Writing - original draft preparation and Writing - review and editing. Conceptualization performed by Zafer Çıplak, Furkan Soysal, and Nuray Yıldız. Methodology realized by Zafer Çıplak and Furkan Soysal. Formal analysis and investigation were carried out by Hasan Altınışık and Bengü Getiren. The study was supervised by Nuray Yıldız.

Data Availability The data generated or analyzed during the present work is available on reasonable request from the corresponding author.

Declarations

Competing Interests The authors have no relevant financial or non-financial interests to disclose.

References

1. C.N. Kedir, D. Salinas-Torres, A.F. Quintero-Jaime, A. Benyoucef, E. Morallon, Journal of Molecular Structure **1248**, (2022)
2. J. Yesuraj, O. Padmaraj, S.A. Suthanthiraraj, J. Inorg. Organomet. Polym Mater. **30**, 310 (2020)
3. A. Soam, R. Kumar, D. Thatoi, M. Singh, J. Inorg. Organomet. Polym Mater. **30**, 3325 (2020)
4. D.J. Ahirrao, A.K. Pal, V. Singh, N. Jha, J. Mater. Sci. Technol. **88**, 168 (2021)
5. A. Borenstein, O. Hanna, R. Attias, S. Luski, T. Brousse, D. Aurbach, J. Mater. Chem. A **5**, 12653 (2017)
6. D.A.L. Almeida, A.B. Couto, N.G. Ferreira, J. Alloys Compd. **788**, 453 (2019)
7. A. Bekhoukh, I. Moulefera, L. Sabantina, B. Abdelghani, Polymers (Basel) **13**, (2021)
8. W. Lyu, M. Yu, J. Feng, W. Yan, Polym. (Guildf) **162**, 130 (2019)
9. H. Li, J. Wang, Q. Chu, Z. Wang, F. Zhang, S. Wang, J. Power Sources **190**, 578 (2009)
10. L. Zhang, X. Qing, Z. Chen, J. Wang, G. Yang, Y. Qian, D. Liu, C. Chen, L. Wang, W. Lei, ACS Appl. Energy Mater. **3**, 6845 (2020)
11. N. Macherla, K. Singh, M.S. Santosh, K. Kumari, R.G.R. Lekkala, Colloids and Surfaces A: Physicochemical and Engineering Aspects **612**, (2021)
12. K. Gholami laelabadi, R. Moradian, I. Manouchehri, ACS Appl. Energy Mater. **4**, 6697 (2021)
13. D.W. Wang, F. Li, J. Zhao, W. Ren, Z.G. Chen, J. Tan, Z.S. Wu, I. Gentle, G.Q. Lu, H.M. Cheng, ACS Nano **3**, 1745 (2009)
14. Y. Meng, K. Wang, Y. Zhang, Z. Wei, Adv. Mater. **25**, 6985 (2013)
15. M.M.M. Ahmed, T. Imae, Phys. Chem. Chem. Phys. **18**, 10400 (2016)
16. K. Jin, W. Zhang, Y. Wang, X. Guo, Z. Chen, L. Li, Y. Zhang, Z. Wang, J. Chen, L. Sun, T. Zhang, Electrochim. Acta **285**, 221 (2018)
17. W.F. Ji, M.M.M. Ahmed, A. Bibi, Y.C. Lee, J.M. Yeh, Electrochimica Acta **390**, (2021)
18. K.M. Ajay, M.N. Dinesh, G. Byatarayappa, M.G. Radhika, N. Kathyayini, H. Vijeth, Inorganic Chemistry Communications **127**, (2021)
19. S.K. Kandasamy, K. Kandasamy, J. Inorg. Organomet. Polym Mater. **28**, 559 (2018)
20. Z. Liu, D. Li, Z. Li, Z. Liu, Z. Zhang, Appl. Surf. Sci. **422**, 339 (2017)
21. J. Liu, P. Du, Q. Wang, D. Liu, P. Liu, Electrochim. Acta **305**, 175 (2019)
22. S. Cho, K.H. Shin, J. Jang, ACS Appl. Mater. Interfaces **5**, 9186 (2013)
23. S. Bilal, B. Begum, S. Gul, A. ul, H.A. Shah, Synth. Met. **235**, 1 (2018)
24. P. Das, S. Mondal, S. Malik, Journal of Energy Storage **39**, (2021)
25. M. Suba Lakshmi, S.M. Wabaidur, Z.A. Alothman, D. Ragupathy, Synthetic Metals **270**, (2020)

26. R. Raccichini, A. Varzi, S. Passerini, B. Scrosati, Nat. Mater. **14**, 271 (2015)
27. L. Sun, L. Wang, C. Tian, T. Tan, Y. Xie, K. Shi, M. Li, H. Fu, RSC Adv. **2**, 4498 (2012)
28. D. Minta, Z. González, P. Wiench, S. Gryglewicz, G. Gryglewicz, Sens. (Switzerland) **20**, 1 (2020)
29. Z. Çıplak, A. Yıldız, N. Yıldız, Journal of Energy Storage **32**, (2020)
30. X. Chen, X. Wang, D. Fang, Fullerenes Nanotubes and Carbon Nanostructures **1048** (2020)
31. L. Wang, Y. Huang, H. Huang, Mater. Lett. **124**, 89 (2014)
32. H. Xu, J. Liu, Y. Chen, C.L. Li, J. Tang, Q. Li, J. Mater. Sci.: Mater. Electron. **28**, 10674 (2017)
33. P.K. Kalambate, C.R. Rawool, S.P. Karna, A.K. Srivastava, Mater. Sci. Energy Technol. **2**, 246 (2019)
34. D. Chen, H. Feng, J. Li, Chem. Rev. **112**, 6027 (2012)
35. H.J. Chu, C.Y. Lee, N.H. Tai, Carbon N Y **80**, 725 (2014)
36. R.K. Upadhyay, N. Soin, G. Bhattacharya, S. Saha, A. Barman, S.S. Roy, Mater. Lett. **160**, 355 (2015)
37. Y. Zhang, J.Y. Zhu, H.B. Ren, Y.T. Bi, L. Zhang, Chin. Chem. Lett. **28**, 935 (2017)
38. K. Gopalakrishnan, S. Sultan, A. Govindaraj, C.N.R. Rao, Nano Energy **12**, 52 (2015)
39. W.D. Wang, X.Q. Lin, H.B. Zhao, Q.F. Lü, J. Anal. Appl. Pyrol. **120**, 27 (2016)
40. G. Liu, Y. Zhou, X. Zhu, Y. Wang, H. Ren, Y. Wang, C. Gao, Y. Guo, Sensors and Actuators, B: Chemical **323**, (2020)
41. T. Autthawong, T. Promanan, B. Chayasombat, A.S. Yu, K. Uosaki, A. Yamaguchi, H. Kurata, T. Chairuangsri, T. Sarakonsri, Crystals (Basel) 11, (2021)
42. P. Bandyopadhyay, T. Kuila, J. Balamurugan, T.T. Nguyen, N.H. Kim, J.H. Lee, Chem. Eng. J. **308**, 1174 (2017)
43. A.M. Kumar, J. Jose, M.A. Hussein, Progress in Organic Coatings **163**, (2022)
44. U. Rana, S. Malik, Chem. Commun. **48**, 10862 (2012)
45. S. Palsaniya, H.B. Nemade, A.K. Dasmahapatra, Journal of Energy Storage **32**, (2020)
46. L. Durc, Z. Mandic, S. Kovac, Electrochimica Acta **40**, (1995)
47. Y. Shen, Z. Qin, T. Li, F. Zeng, Y. Chen, N. Liu, Electrochimica Acta **356**, (2020)
48. Z. Çıplak, N. Yıldız, Synthetic Metals **256**, (2019)
49. N.R. Dywili, A. Ntziouni, C. Ikpo, M. Ndipingwi, N.W. Hlongwa, A.L.D. Yonkeu, M. Masikini, K. Kordatos, E.I. Iwuoha, Micromachines (Basel) **10**, (2019)
50. Y. Gao, J. Ying, X. Xu, L. Cai, Applied Sciences (Switzerland) **8**, (2018)
51. Y. Gawli, A. Banerjee, D. Dhakras, M. Deo, D. Bulani, P. Wadgaonkar, M. Shelke, S. Ogale, Scientific Reports **6**, (2016)
52. N. Macherla, K. Singh, M. Nerella, K. Kumari, and R. G. Reddy Lekkala. Int. J. Energy Res. **46**, 6529 (2022)
53. S.N. Karri, U. Male, P. Srinivasan, Ionics (Kiel) **25**, 191 (2019)